ADVANCED MATERIALS
www.advmat.de

# Architected Liquid Crystal Elastomer Lattices with Programmable Energy Absorption

*Rodrigo Telles, Julie A. Mancini, Jorge-Luis Barrera, Marlini Simoes, Dominique H. Porcincula, Adam Bischoff, Devin J. Roach, Samuel C. Leguizamon, Elaine Lee,* Caitlyn C. Cook,* and Jennifer A. Lewis**

**Architected LCE lattices are fabricated with flow-induced alignment via direct ink writing and systematically characterized their shape morphing, stiffness, and energy absorption behavior across strain rates spanning six orders of magnitude from $10^{-3}$ to $10^{3}$ $s^{-1}$. It is shown that architected liquid crystal elastomer (LCE) lattices exhibit superior energy absorption compared to their non-mesogenic (silicone) counterparts. Importantly, the LCE-to-silicone energy absorption ratios are up to 18-fold higher at the highest strain rate tested. A finite element model that captures their shape-morphing response is developed, which exhibits excellent agreement with the experimental observations. The work opens new avenues for designing and fabricating LCE lattices with programmable alignment, shape morphing, and mechanics.**

## 1. Introduction

Lightweight hierarchical cellular structures have garnered significant attention in recent years due to their ability to combine mechanical efficiency and functionality.[1–3] Nature provides many examples of lightweight architected materials ranging from bird bones to beehive honeycombs. These architectures minimize material use while efficiently distributing loads, absorbing energy, and resisting deformation. In particular, the Bouligand structure, is observed in bone, the dactyl club of the mantis shrimp,[4] bamboo,[5,6] nacre,[7,8] and in the fruit of Pollia condensata.[9] The Bouligand structure, which is composed of unidirectionally aligned fiber lamellae that are helicoidally stacked, provides a natural energy absorbing armor against predators. The log pile structure represents a simplified version in which alternating lamellae are rotated by 90°. With such structures as inspiration, researchers have designed and built architected materials that outperform traditional engineering materials,[10–12] including ultralightweight lattices,[13–15] metamaterials,[16–19] and reconfigurable structures.[20–22]

There is emerging interest in constructing architected matter composed of hierarchical lattices ranging with programmed alignment and geometry across multiple scales. Liquid crystal elastomers (LCEs) are a promising class of soft active materials, which combine the orientational order of liquid crystals with the elastic response of elastomers, enabling them to undergo large and reversible deformations in response to external stimuli, e.g., when heated above their nematic-to-isotropic transition temperature ($T_{NI}$),[23–27] exposed to light[28–30] or an electric field,[31–33] or swelled by solvent.[34–36] LCEs also exhibit unique energy absorption capabilities[37–43] due to their inherently soft elasticity across multiple strain rates.[44,45] Unlike conventional silicone elastomers that exhibit strain-hardening with an increasing load,[46] LCEs remain mechanically soft under large strains due to the presence of liquid crystal mesogens that can collectively reorient in response to an applied load. To date, digital light processing has been primarily used to construct LCE lattices; however, those architectures lack director alignment within their printed struts.[37,43] Recently, thin triangular LCE lattices have been fabricated by direct ink writing (DIW), in which flow-induced alignment is encoded along the printing direction, such that each strut within the lattice exhibits a large contractile strain upon heating above $T_{NI}$.[47–50] DIW has also been used to print solid LCE blocks with enhanced energy absorption capabilities.[39] However, to our

R. Telles, J. A. Lewis
John A. Paulson
School of Engineering and
Applied Sciences
and Wyss
Institute for Biologically Inspired Engineering
Harvard University
Cambridge, MA 02138, USA
E-mail: jalewis@seas.harvard.edu

J. A. Mancini, J.-L. Barrera, D. H. Porcincula, E. Lee, C. C. Cook
Lawrence Livermore National Laboratory
Livermore, CA 94550, USA
E-mail: lee1040@llnl.gov; krikorian3@llnl.gov

M. Simoes
California Institute of Technology
Pasadena, CA 91125, USA

A. Bischoff, D. J. Roach
School of Mechanical
Industrial, and Manufacturing Engineering
Oregon State University
Corvallis, OR 97331, USA

D. J. Roach, S. C. Leguizamon
Advanced Materials Laboratory
Sandia National Laboratories
Albuquerque, NM 87106, USA

The ORCID identification number(s) for the author(s) of this article can be found under https://doi.org/10.1002/adma.202420048

**DOI: 10.1002/adma.202420048**

 

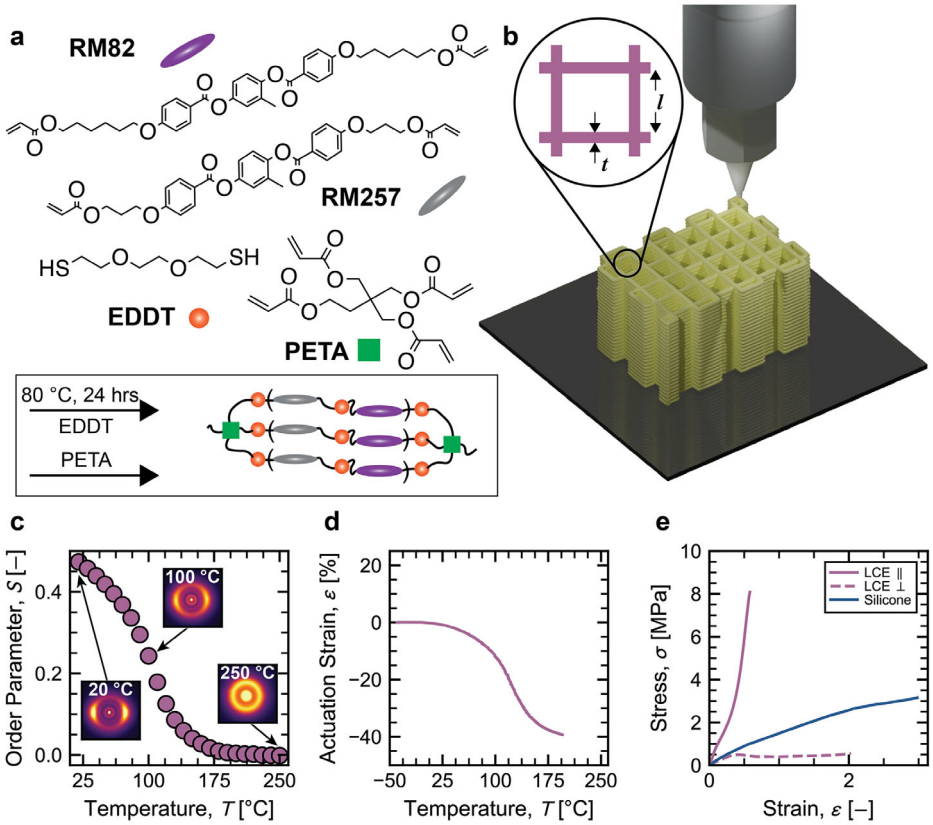


**Figure 1.** Architected LCE lattices. a) LCE ink constituents. b) Schematic illustration of high-aspect ratio, LCE lattice fabricated by direct ink writing. c) Orientational order parameter as a function of temperature. d) Actuation strain of a LCE thick film measured parallel (bottom) to the printing direction. e) Tensile stress–strain response of LCE thick film measured parallel and perpendicular to the printing direction, and a printed silicone thick film (non-mesogenic control). Data are shown as mean ($n \geq 3$).

knowledge, the complex interplay between LCE director alignment, lattice geometry and energy absorption has yet to be investigated over a broad range of strain rates.

Here, we report the direct writing of high-aspect ratio, architected LCE lattices composed of aligned LCE struts with programmable geometry, stiffness, and energy absorption across strain rates spanning six orders of magnitude. By controlling the spacing between printed LCE struts and their director alignment, we systematically investigate the effect of relative density on mechanical performance of 90° log pile structures. To deconvolute the effects of LC alignment from lattice architecture, we produced non-mesogenic silicone lattices in the same configurations. Next, we carried out quasi-static compression measurements on both LCE and silicone lattices as a function of temperature. Their shape morphing response at elevated temperatures ($T > T_{NI}$) is also characterized to elucidate its impact on stiffness and energy absorption. Importantly, we find that the observed energy absorption of architected LCE lattices with a relative density of 49% is 18-fold higher than their silicone counterparts under ambient dynamic loading at the highest strain rate ($10^3$ $s^{-1}$) tested.

## 2. Results and Discussion

Architected lattices are fabricated by printing LCE oligomeric inks via high operating temperature direct ink writing (HOT-DIW).[48] The LCE ink consists of oligomers synthesized from two reactive mesogens RM82 and RM257, and a thiol chain extender via a thiol-Michael addition as well as a tetrafunctional cross-linker added post-oligomerization (**Figure** 1a). Notably, optimizing the cross-linker concentration, 0.1 wt.% of pentaerythritol tetraacrylate, proved to be critical for ensuring fast curing and enabling printing of high-aspect ratio architected LCEs (Figure 1b; Figure S1 and Movie S1, Supporting Information). A fully defined Bouligand lattice consists of six parameters.[51] Here, we focused on a fixed pitch angle of 90°, strut diameter, $t$, and variable spacing between struts, $l$ (Figure 1b, inset). For this geometry, their relative density can be approximated by:[52]

$$\tilde{\rho} = 2\frac{t}{l}\left(1 - \frac{1}{2}\frac{t}{l}\right) \quad (1)$$

The quasi-static compressive behavior of open-cell cellular materials is generally understood to involve three stages:1) linear-elastic response at low strains until the onset collapse or buckling begins, 2) a near-constant stress plateau region, and 3) the densification region.[52] The transition from the linear elastic to plateau region is identified by the onset strain, $\varepsilon_0$, corresponding to the collapse stress, $\sigma_0$. The onset of the densification region, however, has multiple conventions.[53] For our work, we adapt the convention from Tan et al.,[54] where the densification strain, $\varepsilon_D$, is

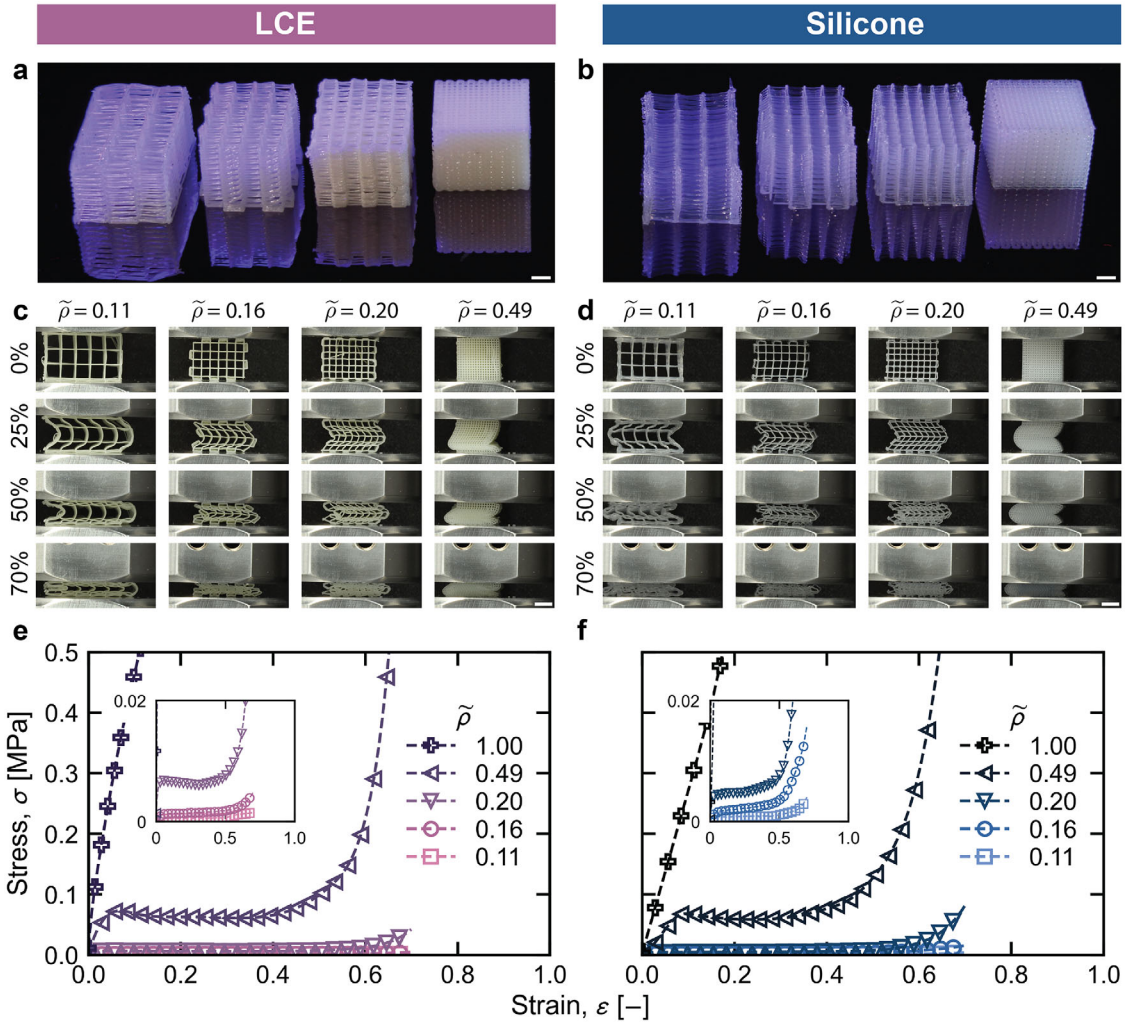


**Figure 2.** Quasi-static compression testing. Optical images of a) LCE and b) silicone 90° log pile lattices with increasing relative densities from left to right. Snapshot images taken during compression testing at 0%, 25%, 50%, and 70% of c) LCE and d) silicone lattice structures, with decreasing relative densities from top to bottom. Compressive stress–strain response of e) LCE and f) silicone lattice structures. (scale bars = 5 mm). Data are shown as mean ($n = 3$).

defined as the maximum energy absorption efficiency, $W(\varepsilon)/\sigma_p$, where $\sigma_p$ is the peak stress and $W$ is the volumetric energy absorption. With a clear definition of the densification strain we can further define the volumetric energy absorption as:

$$W = \int_0^{\varepsilon} \sigma \, d\varepsilon \tag{2}$$

To maximize director alignment, the LCE ink is printed at 35 °C, a temperature that resides between $T_g$ and $T_{NI}$ (Figure S2, Supporting Information), a draw ratio of 1, and $Wi \approx 2.4$ (SI text, Supporting Information). Here, $Wi = \lambda\dot{\gamma}$ is the dimensionless Weissenberg number, defined as a ratio between the longest relaxation time for the ink ($\lambda$) and the processing flow alignment time ($1/\dot{\gamma}$) or inverse shear rate (Figure S3, Supporting Information).[55] Wide-angle X-ray scattering (WAXS) measurements of these samples reveal a scalar orientational order parameter, $S$, of 0.47 at room temperature, which approaches zero when heated above $T_{NI}$ (Figure 1c; Figure S4, Supporting Information), i.e., values comparable to other main-chain LCE inks.[48,56,57] Similarly, normalized contractile actuation strain measurements of ≈40% are observed along the printing direction in uniaxially aligned, thick LCE films (thickness ≈0.5 mm) (Figure 1d) with negligible impact from addition of cross-linker. Their programmed alignment is also apparent in thick LCE films loaded along and orthogonal to printing (alignment) direction, where their stiffness difference is roughly sixfold (Figure 1e). By contrast, the stiffness of printed silicone thick films (non-mesogenic controls) lies within these range of measured values for the LCE films.

To investigate the role of programmed alignment, we printed LCE (**Figure 2a**) and silicone (Figure 2b) lattices with relative densities of 0.11, 0.16, 0.20, 0.49, and 1 (Equation 1). As an initial benchmark, we conducted quasi-static compression measurements at ambient conditions (21 °C) at a strain rate of $10^{-3}$ $s^{-1}$ (Figure 2c,d). The strain rate ($\dot{\varepsilon} = V/H$) is influenced by

the linear velocity ($V$) of the compression platens and the sample thickness ($H$). For these measurements, the lattices are oriented such that the LCE director alignment is along the loading direction. At this loading rate, all lattices exhibited the same global response upon compression: namely, symmetrical buckling about the centerline with the top and bottom lattice rows buckling first, followed by buckling of the centerline row, and ultimately full densification (Figure 2c,d; Figure S5, Supporting Information). Next, we quantified the stress–strain response as a function of relative density for both LCE (Figure 2e) and silicone lattices (Figure 2f). It is well known that in a stress–strain plot, an increase in relative density results in an increased apparent lattice stiffness and a reduced densification strain.[52] We observed similar stress–strain responses for both LCE and silicone lattices, i.e., a linear-elastic response at low strain followed by softening from inception of global buckling, and finally, a sharp increase in stress near the densification strain. The corresponding low-strain Young's modulus is plotted as function of relative density (Figure S6, Supporting Information). For an open-cell cellular solid, the Young's modulus scales as $E \approx \tilde{\rho}^n$, where $n$ is strongly dependent on the lattice architecture, with values between 2 and 3 for bending-dominated structures, and ≈1 for stretch-dominated structures.[52,58,59] We find that the Young's modulus of the LCE lattices scales as $E \approx \tilde{\rho}^{2.81}$, thus exhibiting a highly bending-dominated structure response approaching that of a hexagonal lattice (i.e., $E \approx \tilde{\rho}^3$), whereas the silicone lattices scales as $E \approx \tilde{\rho}^{2.06}$, as expected for an open cell square lattice (i.e., $E \approx \tilde{\rho}^2$). By generating Ashby plots that include values reported in literature,[60–66] we find our lattices span a similar range of normalized Young's moduli as other stochastic foams and architected lattices (Figure S7a, Supporting Information) and slightly lower, absolute values of energy absorption (Figure S7b, Supporting Information).

While the relative density of a given lattice affects its mechanical properties, the ability to tune the global mechanical properties on-the-fly of monolithic structures remains challenging. By harnessing LCE alignment coupled with lattice geometry, stimuli-responsive structures that reversibly shape morph are realized. To demonstrate this, we first show how the porosity of a $\tilde{\rho} = 0.20$ LCE lattice varies as a function of temperature via simulation (**Figure 3a**) and experiment (Figure 3b). Although multiple models have been developed and used to predict the temperature response of LCEs,[49,67,68] we opted for a constitutive model that is a modified version of the LCE material model used by Li and Zhang.[69] The strain energy density for the hyperelastic LCE material considered is given by:

$$\Psi(\bar{F}, J) = \frac{\mu}{2}\left[\frac{1-S_0}{1-S}tr(\bar{C}) + \left(\frac{3S_0}{1+2S} - \omega\right)n_0 \cdot \bar{C}n_0 - \left(\frac{3S(1-S_0)}{(1-S)(1+2S)} - \omega\right)\frac{n_0 \cdot \bar{C}^2 n_0}{n_0 \cdot \bar{C}n_0}\right] + \frac{\kappa}{2}(\ln(J))^2 \quad (3)$$

where $\mu$, $\kappa$, $S$, $\omega$, and $n$ represent the shear modulus, bulk modulus, scalar orientational order parameter, non-ideality parameter, and liquid crystal alignment vector field, respectively. The subscript 0 denotes initial value. The right Cauchy–Green strain tensor $C = F^T F$, is a function of the deformation gradient $F = I + \frac{\partial u}{\partial X}$, where $I$ is the identity tensor, $u$ is the displacement vector, and $X$ is the location of a material particle in the undeformed configuration. In this scenario, the material orientation is determined by the macroscopic deformation. Furthermore, the initial alignment is obtained through $n = Fn_0/|Fn_0|$. To improve convergence, the deformation gradient is averaged using the Fbar method, in which we defined a modified deformation gradient $\bar{F} = -J^{1/3}F$, with $J = \det(F)$ and thus, the strain energy becomes a function of $\bar{C}$. The initial orientational order parameter, $S_0 \geq 0$, indicates the highest possible level of ordering, while $S \in [0, S_0]$ models the nematic ($S = S_0$) to isotropic ( $S = 0$) transition states.

To simulate these printed lattices, the material model introduced above (Equation 3) is implemented in a 3D finite element framework[70,71] that allows for flexible definitions of parameters as domain fields, thus enabling the generation of complex deposition patterns. Using LCE thick films, we interpolated the following material properties from experimental WAXS, actuation strain, and tensile data (Figure 1c–e): $\mu = 4.5 \times 10^6$ Pa, $\kappa = 4.5 \times 10^8$ Pa, $S_0 = 0.47$, and $\omega = 0.125$. In addition, the unit vector $n$ is prescribed as a function of space to emulate alignment along the printing direction (SI Text, Supporting Information). Upon heating, the lattices undergo homogeneous deformation (Figure 3a,b). Finally, by optically tracking the nodal positions as a function of temperature along the $XY$-plane (Figure 3c; Figure S8, Supporting Information) and $XZ$-plane (Figure S9, Supporting Information), we find excellent agreement in global actuation strains along the $X$-, $Y$-, and $Z$-directions (Figure 3d), where the global actuation strains are defined relative to their initial lengths at ambient conditions. Both the $X$- and $Y$-dimensions contract homogeneously to a max contraction of −27%, whereas the Z-dimension expands to roughly half this value to 12%.

Given their directional and areal shape changes as a function of temperature, we next investigated their stress–strain behavior under different thermal conditions. Using an environmental chamber, we subjected the LCE lattice to five different target temperatures—two of which were below, two which were above, and one equal to the inflection temperature (Figure 3d). The stress–strain curve is then computed at each temperature (Figure 3e). Interestingly, the heated compression measurements on the LCE lattices exhibited a similar behavior, as observed for heated tensile testing of LCE thick films.[72] As the temperature increases above room temperature, the overall structure initially softens below $T_{NI}$ prior to stiffening above $T_{NI}$ (Figure 3f), resulting in ≈5-fold change in stiffness akin to other thermally responsive materials[64] and metamaterials that leverage structural instabilities.[66] Similar temperature-dependent behavior is observed for the normalized energy absorption values (Figure 3g). However, unlike most architected materials, the reconfigurability of those based on LCEs enable reversible time-dependent responses based on specific thermo-mechanical environments.

Although these quasi-static measurements provided valuable insights, we must also understand how higher loading rates impact the mechanical performance of the printed lattices. Hence, we evaluated their compressive behavior at both intermediate ($10^{-2}$ – $10^0$ $s^{-1}$) and high ($10^3$ $s^{-1}$) loading rates in the dynamic regime. Akin to quasi-static compressive measurements, the intermediate loading rates are performed using an Instron. Upon increasing the compressive strain rate, their stress–strain curves shift upward (Figure S10, Supporting Information) for both LCE and silicone lattices. We attribute this to the viscoelastic nature

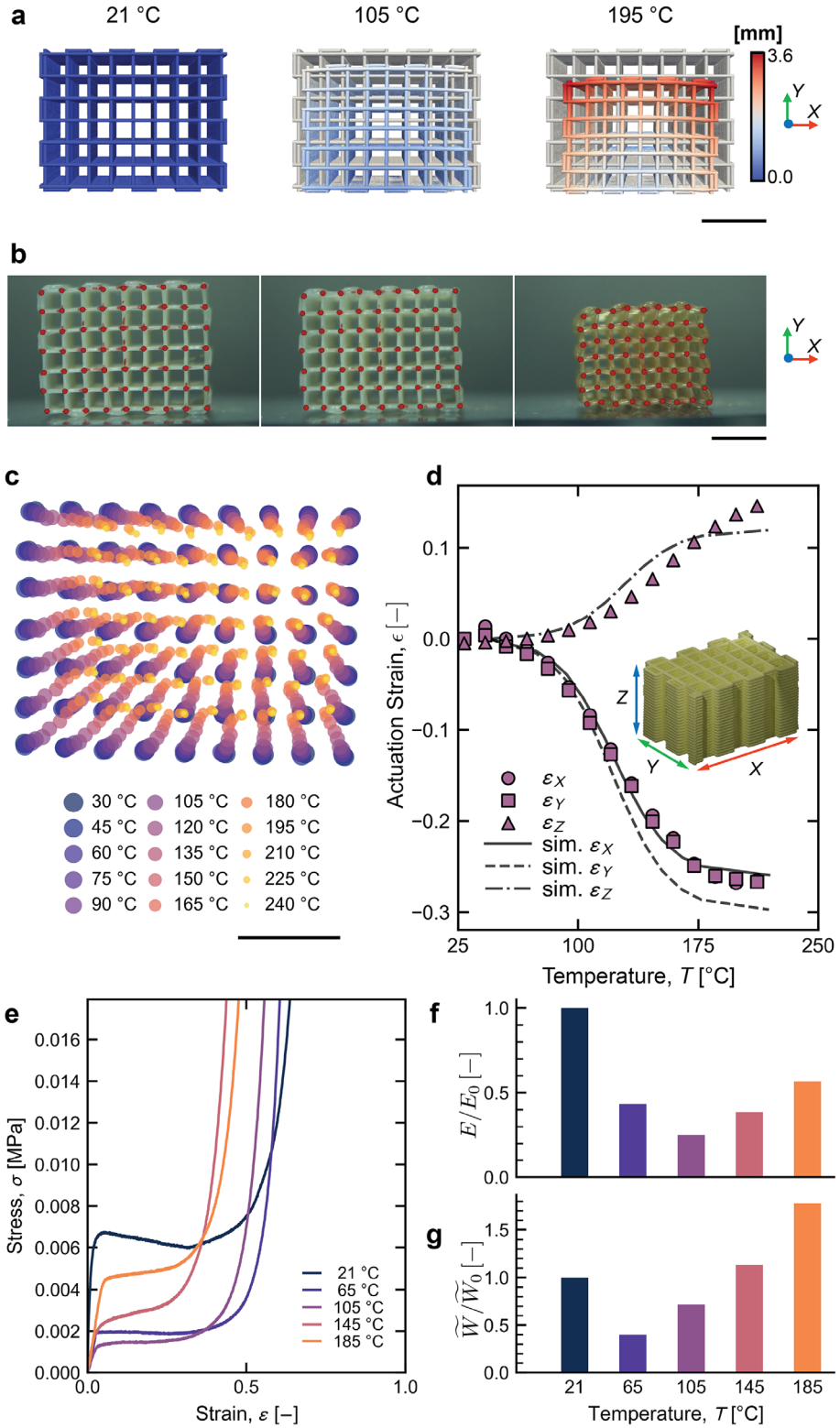


**Figure 3.** Thermally tunable energy absorption. a) Predicted shape change of the *XY*-face of a $\tilde{\rho} = 0.20$ log pile LCE lattice and b) experimentally observed shape change at 21, 105, and 195 °C. Simulation results are color coded based on their displacement magnitude relative to 21 °C. c) Experimentally observed node positions as a function of temperature. d) Global experimental and simulated actuation strains measured along the *X*-, *Y*-, and *Z*-directions. e) Experimentally measured stress–strain response of LCE lattice and their corresponding f) relative Young's modulus and g) energy absorption density as a function of temperature. (scale bars = 5 mm). Data are shown as mean ($n = 3$).

of both elastomers—as strain rate increases, the polymer chains do not have sufficient time to move and adjust, thus resulting in a stiffer and more solid-like response. To probe any delamination during testing, additional cyclic measurements were conducted, and the sample was visually inspected for any irregularities (Figure S11, Supporting Information). As an additional control, we printed a poorly aligned $\tilde{\rho} = 0.49$ LCE lattice at $Wi \approx 0.5$, which exhibits minimal strain-rate dependence akin to the silicone control and further demonstrating the important role of mesogen (Figure S12, Supporting Information). Note, attempts to characterize their behavior at strain rates between $10^1$ and $10^2$ $s^{-1}$ using a drop tower setup were unsuccessful due to the low sensitivity of the accelerometer used.

Next, we investigate the dynamic compressive behavior of the printed LCE and silicone lattices. These measurements are conducted using a split Hopkinson pressure bar (SPHB) (**Figure 4a**). Briefly, this method consists of mounting each sample between two aluminum bars and impacted from one side using an aluminum projectile bar. Upon impact, a roughly square shock wave is transmitted from the incident bar to the sample at a known velocity, $V$, thereby setting the strain rate ($\dot{\epsilon} = V/H$) for a known sample height, $H$. Similar to the quasi-static loading behavior of the LCE lattices (Figure 2c,e; Movie S2, Supporting Information), under dynamic loading, we observe symmetrical buckling about the centerline in the four densest lattices ($\tilde{\rho} = 0.16, 0.20, 0.49, 1$). For the lowest density LCE lattice ($\tilde{\rho} = 0.11$), we observe a shock wave front that initiates at the contacting surface between the sample and the incident bar begins to propagate through the sample as a planar wave front and buckling occurs. (Movie S2, Supporting Information). This dynamic localization behavior is typically observed for cellular structures under dynamic loading at high impact speeds.[73–77] Strikingly, this behavior is exhibited for all the silicone lattices (Movie S2, Supporting Information). During testing, we also captured the secondary effects from the initial shock wave re-propagating through the transmitted bar and back onto the sample (Figure 4b,c). Unlike LCE lattices, such effects are catastrophic for the silicone lattices, which are severely damaged and unusable upon impact. This central observation highlights the benefit of deploying LCE lattices under high strain rate conditions during both single- and multi-impact events.[78] Furthermore, the stress–strain curves quantitatively reveal dramatic differences between the LCE (Figure 4d) and silicone (Figure 4e) lattices for the same relative density. Surprisingly, even the best performing silicone structure (i.e., a solid block ($\tilde{\rho} = 1$) performed similarly to the $\tilde{\rho} = 0.20$ LCE lattice. These results further underscore the important role of director alignment encoded within each printed LCE strut within these architected lattices during HOT-DIW.

As a final performance metric, the energy absorption of all printed lattices across these measured strain rates are compared by assessing their respective LCE-to-silicone normalized energy absorption ratio, $\tilde{W}_{LCE}/\tilde{W}_{silicone}$ (**Figure 5**). This normalization reflects the ratio between the bulk modulus and its corresponding volume, $E_s/V_s$. Under quasi-static conditions, the LCE lattices outperform the silicone lattices with an energy absorption ratio that is two and fourfold higher for the least dense and most dense samples, respectively. This trend of increasing energy absorption ratio is observed at each strain rate, as their relative density increases. This discrepancy is further enhanced as the strain rate approaches the dynamic loading conditions. Under those conditions, the inception of a shock wave propagating through the $\tilde{\rho} = 0.11$ LCE lattice, results in a slight decrease in the energy absorption ratio compared to a strain rate of $10^0$ $s^{-1}$. However, the other four LCE lattices ($\tilde{\rho} > 0.11$) where stress localization is not observed exhibit a far higher energy absorption capacity resulting in a ≈ 10x to 40x enhancement in energy absorption for architected LCE lattices compared to their non-mesogenic silicone lattices, which serve as controls. Under certain conditions, fully dense LCE lattices ($\tilde{\rho} = 1$) outperform their lower relative density counterparts. When material cost or weight is constrained, open lattices are preferred. Moreover, we anticipate that more bending-dominated geometries, such as those based on triangular or re-entrant honeycomb lattices, would exhibit enhanced energy absorption at even lower densities. Given the scalable synthesis of LCE inks and the use of hyperbolic nozzles on printing well aligned LCE filaments ($Wi \gg 1$),[55] we anticipate that far larger architectures could be rapidly generated, akin to big area additive manufacturing (BAAM).[79]

## 3. Conclusion

In summary, we have printed LCE lattices with programmed director alignment and geometry and systematically characterized their stiffness and energy absorption capability across strain rates spanning six orders of magnitude. Well aligned LCE lattices exhibit superior energy absorption compared to their non-mesogenic (silicone) and poorly aligned LCE counterparts over the broad range of relative densities explored. We implemented a finite element model that captures their shape-morphing response and exhibits excellent agreement with the experimentally observed behavior. Our work opens new avenues for designing and fabricating architected LCE lattices with programmable alignment, stiffness, and energy absorption.

## 4. Experimental Section

*LCE and Silicone Inks*: All reagents were used without additional purification unless otherwise noted. The liquid crystalline oligomer ink was synthesized by a one-pot thiol-Michael addition synthesis. To a 25 mL scintillation vial, difunctional liquid crystal mesogens 1,4-Bis-[4-(6-acryloyloxyhexyloxy)benzoyloxy]-2-methylbenzene (RM82; Synthon, 96%) and 1,4-Bis-[4-(3-acryloyloxypropyloxy)benzoyloxy]-2-methylbenzene (RM257; Synthon, 97%), 2,2′-(ethylenedioxy)diethanethiol (EDDT; Sigma–Aldrich, 95%) were combined with 1 wt.% triethylamine (Sigma–Aldrich, ≥99.95%) and 2 wt.% butylated hydroxytoluene (Sigma–Aldrich, ≥99%) and heated at 80 °C until melted. The overall acrylate to thiol molar ratio was 1.0:0.75, with the acrylate composition consisting of 25 wt.% RM257 and 75 wt.% RM82. The reaction was heated to 65°C for 24 h after which 1.5 wt.% 2,2-dimethoxy-2-phenylacetophenone (Sigma–Aldrich, >99%) and 0.1 wt.% pentaerythritol tetraacrylate (PETA; Sigma–Aldrich) was added and mixed into the oligomer mixture through a series of heating to 65 °C and stirring steps. The silicone ink consists of a weight ratio of 10:1 SE1700 base:SE1700 curing agent (Dow) and was prepared by centrifugal mixing at 2000 rpm for 2 min (FlackTek).

*Differential Scanning Calorimetry (DSC)*: Samples for DSC were prepared by loading ≈10 mg of oligomer ink sample in Tzero aluminum hermetic pans. Under nitrogen flow the polymers were heated to 150 °C to erase any thermal history, held for 10 min, followed by two cycles of cooling to − 50 °C and heating to 150 °C at a ramp rate of 10 °C $min^{-1}$ (DSC 2500, TA Instruments). Data shown from the second heating cycle.

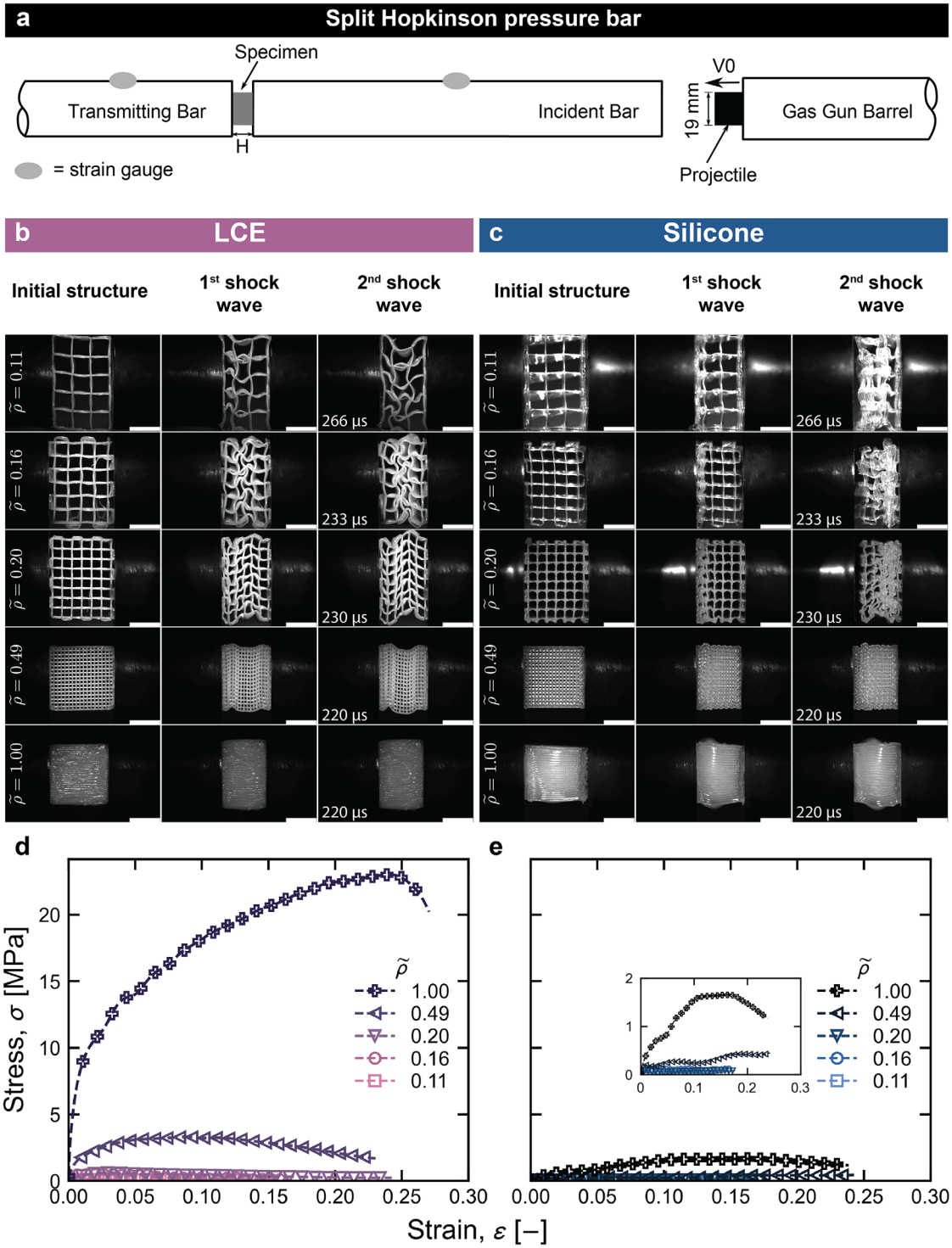


**Figure 4.** High strain, dynamic compression testing. a) Schematic of split Hopkinson pressure bar (SHPB) used to generate high strain rates. b) Snapshot images during dynamic loading of LCE and c) silicone log pile lattice structures at rest, after 1st shock wave, and after 2nd shock wave. The relative densities increase from top to bottom and the impact is from left to right. d) Compressive stress–strain response of LCE and e) silicone lattice structures. (scale bars = 5 mm). Data are shown as mean ($n = 2$).

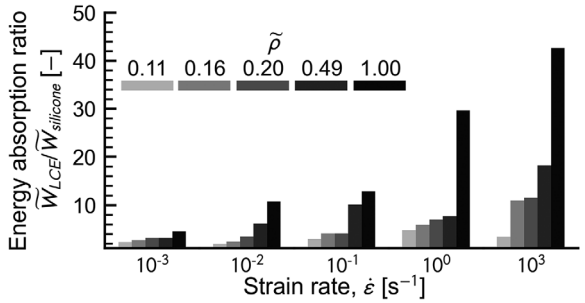


**Figure 5.** LCE lattices exhibit superior energy absorption. Plot of energy absorption density ratio relative of LCE-to-silicone lattices of varying relative densities as a function of strain rate spanning from the quasi-static to dynamic loading regime.

*Rheology*: Rheological properties of the LCE inks were characterized using a controlled stress rheometer (Discovery HR-2 Hybrid Rheometer, TA Instruments) equipped with a 20 mm steel Peltier parallel plate geometry and a 0.250 mm gap. Prior to testing, the ink was brought above the $T_{NI}$ to erase thermal history then cooled to 35 °C. UV rheology was performed with a broadband light source (S2000, Omnicure) at an intensity of ≈30 mW $cm^{-2}$. Samples were irradiated between a 20 mm aluminum top plate and 20 mm acrylic bottom plate, with a 0.250 mm gap. Oscillatory motion was applied in the linear viscoelastic regime at a 0.1% strain with frequency of 1 Hz for up to 90 s. Oscillatory motion was conducted in the dark for the first 30 s, followed by UV illumination for the remaining 60 s. Gel time was determined through the crossover point between storage and loss modulus.

*3D Printing*: LCE and silicone log pile lattices were printed using a custom HOT-DIW setup. Briefly, a machined copper block with an RTD sensor (Omega) and two 100-watt cartridge heaters (Omega) provide closed-loop temperature control via an Omega platinum series single zone temperature controller. Each ink was loaded into a 3 cc stainless steel barrel with a 250 µm stainless steel nozzle (Tecdia) coupled to a Nordson 3 cc high pressure adapter (Nordson). The printhead was mounted onto a custom three-axis motion control stage (Aerotech Inc.) that uses an Ultimus V pressure box (Nordson) to deposit LCE ink. Printing heights are set equal to the diameter of the nozzle and printing speeds are set to match the ink extrudate velocity, unless otherwise specified. During printing, LCE filaments are cured in situ (Omnicure S2000 with 320–500 nm filter, Excelitas) at ≈ 30 mW $cm^{-2}$ (PM100D, ThorLabs), followed by a 30-min post cure on each side at 12 mW $cm^{-2}$ (XYZprinting, Inc). Silicone prints were thermally cured after printing in an oven at 150 °C for 16 h. G-code generation and custom automation scripts were programmed using open-sourced Python libraries (Mecode).

*Mechanical Testing*: Compression tests were performed on an Instron 5943 equipped with a 1 kN load cell and 50 mm diameter stainless steel platens, and operated at strain rates $10^{-3}$, $10^{-2}$, $10^{-1}$, and $10^{0}$ $s^{-1}$. Sample dimensions were measured before each test after thermally cycling above $T_{NI}$ to remove any thermal history in the LCE lattices. Elevated temperature measurements were conducted with an an environmental chamber (3119-403, Instron). Each sample was allowed to reach thermal equilibrium by holding at the target temperature for 10 min. A type-J thermocouple affixed to the compression platens was used to actively record the true sample temperature versus the nominal environmental chamber reported temperature value.

*Dynamic Testing*: The dynamic compression tests were conducted with a split Hopkinson pressure bar (SHPB) testing setup. The incident bar is solid, made of aluminum 7075 with a length of 6 feet, and diameter of 0.75 inches. The transmitted bar is hollow, made of aluminum 6061, with a length of 3 feet and the same diameter as the incident bar. Samples were mounted in between the two bars and impacted by a 0.4 kg, 18 in long solid cylindrical aluminum 7075 projectile of the same diameter as the bars. The projectile is fired from a gas gun at 30 psi. To eliminate bar bending effects, both the incident and transmitted bars are equipped with a pair of strain gauges that are mounted diametrically opposite one another. Real-time images of sample deformation are acquired using a high-speed camera (HPV-X2, Shimadzu) at capture rates up to 150150 frames per second (fps).

*Thermomechanical Characterization*: The deformation of LCE thick films (uniaxially aligned controls, Figure 1d) with approximate dimensions of 20 mm × 5 mm × 0.5 mm as a function of temperature was measured using a a dynamic mechanical analyzer (Q850, TA Instruments) equipped with an ACS-3 refrigerated air supply using the controlled force method. Using a 0.01 N preload and 0 N dynamic force during testing, samples were heated to 200 °C to erase thermal history, held for five minutes, cooled to 0 °C, and heated to 200 °C at a ramp rate of 10 °C $min^{-1}$. Data shown from second heating cycle. The shape change behavior of each log pile lattice structure was measured optically (Canon EOS Rebel T5) by marking nodes with a red marker prior to heating inside an environmental chamber (3119-403, Instron). Each sample was allowed to reach thermal equilibrium by holding at the target temperature for 5 min. Node tracking was performed using a custom Python script based on OpenCV.

*Wide-Angle X-Ray Scattering*: X-ray measurements were performed in transmission mode on a laboratory X-ray beamline Xeuss 3.0 (Xenocs Inc.) equipped with a temperature control stage (HFSX350, Linkham). Scattering patterns were measured at 8.04 keV (Cu-K$\alpha$ source) with a beam spot size of ≈1.4 mm, exposure time of 300 s, and recorded on a Eiger 2R 1M detector (Dectris). Sample-to-detector distance calibrations were performed using a lanthanum hexaboride ($LaB_6$, simple cubic) diffraction standard. All analysis presented used a single "stitched" scattering pattern, comprised of measurments collected at multiple detector positions to remove detector gaps. Scalar orientational order parameters, $S =< P_2(\cos\chi) >$, were calculated by extracting the mesogen scattering peak intensity (0.7 – 2.1 $Å^{-1}$) as a function of azimuthal angle. Data processing and stitching were performed using custom Python scripts based on pyFAI.[80]

*Statistical Analysis*: All raw data were plotted and analyzed using open-source Python libraries Matplotlib and Numpy, where applicable, averages and standard deviations are used and reported in the figure captions along with the sample size (n).

## Supporting Information

Supporting Information is available from the Wiley Online Library or from the author.

## Acknowledgements

The authors gratefully acknowledge support from the ARO MURI program (W911NF-22-1-0219) and the National Science Foundation through the Harvard MRSEC (DMR-2011754). This work was performed under the auspices of the US Department of Energy by Lawrence Livermore National Laboratory under contract DE-AC52-07NA27344, LDRD tracking number 22-ERD-030 and 25-SI-005, and release number LLNL-JRNL-870149. Sandia National Laboratories is a multimission laboratory managed and operated by National Technology & Engineering Solutions of Sandia, LLC, a wholly owned subsidiary of Honeywell International Inc., for the U.S. Department of Energy's National Nuclear Security Administration under contract DE-NA0003525. The authors would also like to thank A. Fergerson and E.C. Davidson for running heated WAXS experiments and J. Muhammad, M.K. Abdelrahman, A. Wat, M.J. Ford, and A.E. Gongora for helpful discussions.

## Conflict of Interest

The authors declare no conflict of interest.

## Author Contributions

R.T., D.J.R., E.L., C.C.C., and J.A.L. conceived the idea and D.J.R., S.C.L., E.L., C.C.C., and J.A.L. supervised research project. R.T. performed all sample and mechanical characterization and data analysis. D.H.P. synthesized LCEs. R.T. and J.A.M. performed 3D printing and toolpath generation. A.B. and D.J.R. assisted with drop tower setup and characterization. J.L.B. conducted numerical shape change simulations. M.S. performed dynamic impact measurements. R.T. and J.A.L. wrote the manuscript. All authors reviewed and approved the final manuscript.

## Data Availability Statement

The data that support the findings of this study are available from the corresponding author upon reasonable request.

## Keywords

active lattices, direct ink writing, energy absorption, liquid crystal elastomers, shape morphing

Received: December 19, 2024
Revised: June 6, 2025
Published online:

[1] A. G. Evans, J. W. Hutchinson, N. A. Fleck, M. F. Ashby, H. N. G. Wadley, *Prog. Mater. Sci.* **2001**, *46*, 309.
[2] H. N. G. Wadley, *Philos. Transact. A Math. Phys. Eng. Sci.* **2006**, *364*, 31.
[3] Y. Wang, L. Li, D. Hofmann, J. E. Andrade, C. Daraio, *Nature* **2021**, *596*, 238.
[4] J. C. Weaver, G. W. Milliron, A. Miserez, K. Evans-Lutterodt, S. Herrera, I. Gallana, W. J. Mershon, B. Swanson, P. Zavattieri, E. DiMasi, D. Kisailus, *Science* **2012**, *336*, 1275.
[5] A. Muhammad, M. d. R. Rahman, S. Hamdan, K. Sanaullah, *Polym. Bull.* **2019**, *76*, 2655.
[6] A. K. Ray, S. Mondal, S. K. Das, P. Ramachandrarao, *J. Mater. Sci.* **2005**, *40*, 5249.
[7] B. Ji, H. Gao, *Annu. Rev. Mater. Res.* **2010**, *40*, 77.
[8] R. Wang, H. S. Gupta, *Annu. Rev. Mater. Res.* **2011**, *41*, 41.
[9] S. Vignolini, P. J. Rudall, A. V. Rowland, A. Reed, E. Moyroud, R. B. Faden, J. J. Baumberg, B. J. Glover, U. Steiner, *Proc. Natl. Acad. Sci., U. S. A.* **2012**, *109*, 15712.
[10] T. A. Schaedler, W. B. Carter, *Annu. Rev. Mater. Res.* **2016**, *46*, 187.
[11] W. P. Moestopo, A. J. Mateos, R. M. Fuller, J. R. Greer, C. M. Portela, *Adv. Sci.* **2020**, *7*, 2001271.
[12] C. M. Portela, A. Vidyasagar, S. Krödel, T. Weissenbach, D. W. Yee, J. R. Greer, D. M. Kochmann, *Proc. Natl. Acad. Sci., U. S. A.* **2020**, *117*, 5686.
[13] T. A. Schaedler, A. J. Jacobsen, A. Torrents, A. E. Sorensen, J. Lian, J. R. Greer, L. Valdevit, W. B. Carter, *Science* **2011**, *334*, 962.
[14] X. Zheng, H. Lee, T. H. Weisgraber, M. Shusteff, J. DeOtte, E. B. Duoss, J. D. Kuntz, M. M. Biener, Q. Ge, J. A. Jackson, S. O. Kucheyev, N. X. Fang, C. M. Spadaccini, *Science* **2014**, *344*, 1373.
[15] C. M. Portela, B. W. Edwards, D. Veysset, Y. Sun, K. A. Nelson, D. M. Kochmann, J. R. Greer, *Nat. Mater.* **2021**, *20*, 1491.
[16] K. Bertoldi, V. Vitelli, J. Christensen, M. van Hecke, *Nat. Rev. Mater.* **2017**, *2*, 17066.
[17] J. Bauer, L. R. Meza, T. A. Schaedler, R. Schwaiger, X. Zheng, L. Valdevit, *Adv. Mater.* **2017**, *29*, 1701850.
[18] L. R. Meza, A. J. Zelhofer, N. Clarke, A. J. Mateos, D. M. Kochmann, J. R. Greer, *Proc. Natl. Acad. Sci., U. S. A.* **2015**, *112*, 11502.
[19] X. Zheng, W. Smith, J. Jackson, B. Moran, H. Cui, D. Chen, J. Ye, N. Fang, N. Rodriguez, T. Weisgraber, C. M. Spadaccini, *Nat. Mater.* **2016**, *15*, 1100.
[20] X. Xia, C. M. Spadaccini, J. R. Greer, *Nat. Rev. Mater.* **2022**, *7*, 683.
[21] S. Shan, S. H. Kang, J. R. Raney, P. Wang, L. Fang, F. Candido, J. A. Lewis, K. Bertoldi, *Adv. Mater.* **2015**, *27*, 4296.
[22] B. Haghpanah, L. Salari-Sharif, P. Pourrajab, J. Hopkins, L. Valdevit, *Adv. Mater.* **2016**, *28*, 7915.
[23] T. H. Ware, M. E. McConney, J. J. Wie, V. P. Tondiglia, T. J. White, *Science* **2015**, *347*, 982.
[24] J. Küpfer, H. Finkelmann, *Makromol. Chem. Rapid Commun.* **1991**, *12*, 717.
[25] T. H. Ware, T. J. White, *Polym. Chem.* **2015**, *6*, 4835.
[26] A. Kotikian, C. McMahan, E. C. Davidson, J. M. Muhammad, R. D. Weeks, C. Daraio, J. A. Lewis, *Sci. Robot.* **2019**, *4*, aax7044.
[27] A. Kotikian, J. M. Morales, A. Lu, J. Mueller, Z. S. Davidson, J. W. Boley, J. A. Lewis, *Adv. Mater.* **2021**, *33*, 2101814.
[28] S. Palagi, A. G. Mark, S. Y. Reigh, K. Melde, T. Qiu, H. Zeng, C. Parmeggiani, D. Martella, A. Sanchez-Castillo, N. Kapernaum, Giesselmann, F., D. S. Wiersma, E. Lauga, P. Fischer, *Nat. Mater.* **2016**, *15*, 647.
[29] Y. Yu, M. Nakano, T. Ikeda, *Nature* **2003**, *425*, 145.
[30] A. W. Hauser, D. Liu, K. C. Bryson, R. C. Hayward, D. J. Broer, *Macromolecules* **2016**, *49*, 1575.
[31] H. E. Fowler, P. Rothemund, C. Keplinger, T. J. White, *Adv. Mater.* **2021**, *33*, 2103806.
[32] C. Zhang, G. Chen, K. Zhang, B. Jin, Q. Zhao, T. Xie, *Adv. Mater.* **2024**, *36*, 2313078.
[33] V. Maurin, Y. Chang, Q. Ze, S. Leanza, J. Wang, R. R. Zhao, *Adv. Mater.* **2024**, *36*, 2302765.
[34] K. D. Harris, C. W. M. Bastiaansen, D. J. Broer, *J. Microelectromechanical Syst.* **2007**, *16*, 480.
[35] J. M. Boothby, H. Kim, T. H. Ware, *Sens. Actuators, B* **2017**, *240*, 511.
[36] D. S. Kim, Y.-J. Lee, Y. Wang, J. Park, K. I. Winey, S. Yang, *ACS Appl. Mater. Interfaces* **2022**, *14*, 50171.
[37] C. Luo, C. Chung, N. A. Traugutt, C. M. Yakacki, K. N. Long, K. Yu, *ACS Appl. Mater. Interfaces* **2021**, *13*, 12698.
[38] B. Song, D. Landry, T. Martinez, C. N. Chung, K. N. Long, K. Yu, C. M. Yakacki, *Mech. Mater.* **2024**, *197*, 105086.
[39] D. Mistry, N. A. Traugutt, B. Sanborn, R. H. Volpe, L. S. Chatham, R. Zhou, B. Song, K. Yu, K. N. Long, C. M. Yakacki, *Nat. Commun.* **2021**, *12*, 6677.
[40] D. R. Merkel, R. K. Shaha, C. M. Yakacki, C. P. Frick, *Polymer* **2019**, *166*, 148.
[41] C. P. M. Linares, N. A. Traugutt, M. O. Saed, A. M. Linares, C. M. Yakacki, T. D. Nguyen, *Soft Matter* **2020**, *16*, 8782.
[42] S.-Y. Jeon, B. Shen, N. A. Traugutt, Z. Zhu, L. Fang, C. M. Yakacki, T. D. Nguyen, S. H. Kang, *Adv. Mater.* **2022**, *34*, 2200272.
[43] N. A. Traugutt, D. Mistry, C. Luo, K. Yu, Q. Ge, C. M. Yakacki, *Adv. Mater.* **2020**, *32*, 2000797.
[44] M. Warner, E. M. Terentjev, *Liquid Crystal Elastomers*, Oxford University Press, Oxford, New York **2003**.
[45] A. Bischoff, C. Bawcutt, M. Sorkin, J. Yazzie, C. C. Cook, S. C. Leguizamon, A. W. Cook, D. J. Roach, *Adv. Eng. Mater.* **2025**, *27*, 2401796.
[46] T. K. Kim, J. K. Kim, O. C. Jeong, *Microelectron. Eng.* **2011**, *88*, 1982.
[47] M. O. Saed, C. P. Ambulo, H. Kim, R. De, V. Raval, K. Searles, D. A. Siddiqui, J. M. O. Cue, M. C. Stefan, M. R. Shankar, T. H. Ware, *Adv. Funct. Mater.* **2019**, *29*, 1806412.
[48] A. Kotikian, R. L. Truby, J. W. Boley, T. J. White, J. A. Lewis, *Adv. Mater.* **2018**, *30*, 1706164.
[49] A. Kotikian, A. A. Watkins, G. Bordiga, A. Spielberg, Z. S. Davidson, K. Bertoldi, J. A. Lewis, *Adv. Mater.* **2024**, *36*, 2310743.

[50] C. P. Ambulo, J. J. Burroughs, J. M. Boothby, H. Kim, M. R. Shankar, T. H. Ware, *ACS Appl. Mater. Interfaces* **2017**, *9*, 37332.
[51] I. M. Van Meerbeek, J. M. Lenhardt, W. Small, T. M. Bryson, E. B. Duoss, T. H. Weisgraber, *MRS Bull.* **2022**, *48*, 325.
[52] L. J. Gibson, M. F. Ashby, *Cellular Solids: Structure and Properties*, Cambridge University Press, Cambridge, England **1997**.
[53] Q. M. Li, I. Magkiriadis, J. J. Harrigan, *J. Cell. Plast.* **2006**, *42*, 371.
[54] P. J. Tan, J. J. Harrigan, S. R. Reid, *Mater. Sci. Technol.* **2002**, *18*, 480.
[55] R. Telles, A. Kotikian, G. Freychet, M. Zhernenkov, P. Wąsik, B. M. Yavitt, J.-L. Barrera, C. C. Cook, R. Pindak, E. C. Davidson, J. A. Lewis, *Proc. Natl. Acad. Sci., U. S. A.* **2025**, *122*, 2414960122.
[56] G. E. Bauman, J. D. Hoang, M. F. Toney, T. J. White, *ACS Macro Lett.* **2023**, *12*, 248.
[57] E. C. Davidson, A. Kotikian, S. Li, J. Aizenberg, J. A. Lewis, *Adv. Mater.* **2020**, *32*, 1905682.
[58] N. A. Fleck, V. S. Deshpande, M. F. Ashby, *Proc. R. Soc. Math. Phys. Eng. Sci.* **2010**, *466*, 2495.
[59] V. S. Deshpande, M. F. Ashby, N. A. Fleck, *Acta Mater.* **2001**, *49*, 1035.
[60] L. R. Meza, S. Das, J. R. Greer, *Science* **2014**, *345*, 1322.
[61] A. G. Evans, M. Y. He, V. S. Deshpande, J. W. Hutchinson, A. J. Jacobsen, W. B. Carter, *Int. J. Impact Eng.* **2010**, *37*, 947.
[62] A. Guell Izard, J. Bauer, C. Crook, V. Turlo, L. Valdevit, *Small* **2019**, *15*, 1903834.
[63] J. Bauer, J. A. Kraus, C. Crook, J. J. Rimoli, L. Valdevit, *Adv. Mater.* **2021**, *33*, 2005647.
[64] F. Deng, Q.-K. Nguyen, P. Zhang, *Appl. Mater. Today* **2022**, *29*, 101671.
[65] D. Restrepo, N. D. Mankame, P. D. Zavattieri, *Extreme Mech. Lett.* **2015**, *4*, 52.
[66] W. Liu, S. Janbaz, D. Dykstra, B. Ennis, C. Coulais, *Nature* **2024**, *634*, 842.
[67] S. Li, G. Librandi, Y. Yao, A. J. Richard, A. Schneider-Yamamura, J. Aizenberg, K. Bertoldi, *Adv. Mater.* **2021**, *33*, 2105024.
[68] R. Brighenti, C. G. McMahan, M. P. Cosma, A. Kotikian, J. A. Lewis, C. Daraio, *Int. J. Solids Struct.* **2021**, *219–220*, 92.
[69] W. Li, X. S. Zhang, *Comput. Methods Appl. Mech. Eng.* **2023**, *417*, 116393.
[70] J. L. Barrera, C. Cook, E. Lee, K. Swartz, D. Tortorelli, *Polymers* **2024**, *16*, 1425.
[71] R. Anderson, J. Andrej, A. Barker, J. Bramwell, J.-S. Camier, J. Cerveny, V. Dobrev, Y. Dudouit, A. Fisher, T. Kolev, W. Pazner, M. Stowell, V. Tomov, I. Akkerman, J. Dahm, D. Medina, S. Zampini, *Comput. Math. Appl.* **2021**, *81*, 42.
[72] H. Finkelmann, A. Greve, M. Warner, *Eur. Phys. J. E* **2001**, *5*, 281.
[73] A. T. Barnes, K. Ravi-Chandar, S. Kyriakides, S. Gaitanaros, *Int. J. Solids Struct.* **2014**, *51*, 1631.
[74] S. Lee, F. Barthelat, N. Moldovan, H. D. Espinosa, H. N. G. Wadley, *Int. J. Solids Struct.* **2006**, *43*, 53.
[75] Z. Zheng, J. Yu, J. Li, *Int. J. Impact Eng.* **2005**, *32*, 650.
[76] D. Ruan, G. Lu, B. Wang, T. X. Yu, *Int. J. Impact Eng.* **2003**, *28*, 161.
[77] P. J. Tan, S. R. Reid, J. J. Harrigan, Z. Zou, S. Li, *J. Mech. Phys. Solids* **2005**, *53*, 2174.
[78] E. C. Clough, T. A. Plaisted, Z. C. Eckel, K. Cante, J. M. Hundley, T. A. Schaedler, *Matter* **2019**, *1*, 1519.
[79] A. Roschli, K. T. Gaul, A. M. Boulger, B. K. Post, P. C. Chesser, L. J. Love, F. Blue, M. Borish, *Addit. Manuf.* **2019**, *25*, 275.
[80] J. Kieffer, D. Karkoulis, *J. Phys. Conf. Ser.* **2013**, *425*, 202012.